




Cite this: *J. Mater. Chem. C*, 2017, 5, 4884

## Gold mesoflowers with a high density of multilevel long sharp tips: synthesis and characterization†

Nhung Thi Tran,<sup>ab</sup> Anran Li,<sup>bc</sup> Peng Chen,<sup>ab</sup> Yi Wang,<sup>ad</sup> Shuzhou Li<sup>b</sup> and Bo Liedberg <sup>\*ab</sup>

A one-step, aqueous-based, and surfactant-free method to synthesize gold mesoflowers (AuMFs) with multilevel long sharp tips is reported. The method enables control of the size, morphology, and optical properties of the AuMFs by tuning the reaction parameters such as concentration of precursor, halide, and reducing agent. The nanoparticle growth process is studied in detail and our findings suggest that chloride ions play a decisive role in the formation of long sharp tips and tip branching. The synthesized particles exhibit a tunable localized surface plasmon resonance (LSPR) response in the NIR and MIR regions (~1800–3000 nm). These experimental observations are in agreement with simulations based on the finite-difference time-domain (FDTD) method. Moreover, the simulations also point towards a highly morphology-dependent field enhancement that opens up future applications of the AuMFs in surface-enhanced vibrational spectroscopy and sensing/therapeutics.

Received 6th March 2017,  
Accepted 25th April 2017

DOI: 10.1039/c7tc00968b

rsc.li/materials-c

### Introduction

Complex anisotropic metal nanoparticles have attracted intensive research interest due to their unique optical properties arising from the localized surface plasmon resonance (LSPR) phenomenon.<sup>1–3</sup> Particularly, the ability to concentrate light at the nanometer length scale, fine tune the LSPR peak across a wide spectral range, and enhance the local electromagnetic (EM) field makes such particles promising candidates for surface enhanced vibrational spectroscopy (surface enhanced Raman scattering SERS and surface enhanced IR absorbance SEIRA) as well as for sensing/therapeutic applications.<sup>1,4–10</sup> To date, various types of metal nanoparticles with complex morphologies have been prepared such as meatball, hierarchical, nanostar, multipod, sea urchin, nanotexture, *etc.*<sup>2,9,11–15</sup> Most of these metal nanoparticles exhibit LSPR peaks in the visible to NIR regions, ranging up to ~2000 nm. However, for molecular spectroscopy using SEIRA, one requires that plasmon excitation is further pushed into the

MIR region.<sup>1,4–10</sup> Therefore, it is appealing to fabricate novel and complex metal nanoparticles with tunable optical properties.

The extinction spectrum of noble metal nanoparticles can be tuned by engineering their size, shape, composition and inter-particle distance.<sup>16–19</sup> Among the different classes of shape-engineered nanoparticles, branched gold nanoparticles, including nanostars, nanourchins, spiky balls, *etc.*, have recently attracted tremendous attention.<sup>6,20,21</sup> Due to the high charge density and charge polarization at small-radii tip extremities, branched gold nanoparticles provide a huge enhancement of the local EM field and a tunable LSPR peak over a wide spectral range.<sup>21–23</sup> Numerous experiments and simulations have been performed to elucidate the LSPR properties including the huge local EM enhancement of branched gold nanoparticles at the nanoscale. However, mesoscale branched gold particles have not been studied in detail.<sup>10,16,24</sup> According to Feng Hao and co-workers, the core of branched gold nanoparticles serves as a nanoscale antenna for the tips, which enhances the excitation cross-section as well as the local EM field.<sup>24,25</sup> In addition, the length, sharpness, and the density of tips also influence the LSPR properties.<sup>21,26</sup> For example, a red-shift of the LSPR peak position is expected when the tip length and/or tip sharpness increases.<sup>26–28</sup> However, anisotropic growth of long sharp tips is not energetically favored in solution because of the high surface energy and the high symmetry in face centered cubic (fcc) metal crystals.<sup>17</sup> The atoms at the tip tend to dissolve and rearrange to form roughened protrusions (truncations) upon formation or during storage because of the Ostwald ripening effect.<sup>27</sup> It is noteworthy that controlled synthesis of multilevel branched particles is challenging and only a few examples have

<sup>a</sup> Centre for Biomimetic Sensor Science, 50 Nanyang Drive, Singapore 637553

<sup>b</sup> School of Materials Science and Engineering, Nanyang Technological University, Singapore 639798. E-mail: bliedberg@ntu.edu.sg

<sup>c</sup> School of Chemistry and Environment, Beihang University, Beijing, P. R. China

<sup>d</sup> Wenzhou Institute of Biomaterials and Engineering, Chinese Academy of Sciences, Wenzhou, Zhejiang, China

† Electronic supplementary information (ESI) available: Element mapping and EDX spectrum of AuMFs, TEM images of gold nanostars synthesized by replacing HCl with H<sub>2</sub>SO<sub>4</sub>, TEM images of different tip branching levels, SEM and TEM images of AuMFs synthesized by adding 120 µL NaCl (1.0 M) stock solution, SEM images of AuMFs at different growth stages, and a table summarizing all the simulated results. See DOI: 10.1039/c7tc00968b

been reported.<sup>8,29</sup> For example, Yuan *et al.* exploited a multistep protocol of seed-mediated growth approach to grow multilevel 3D gold particles with long thorns.<sup>8</sup> They proposed that AgNO<sub>3</sub> contributed decisively to the growth of multilevel gold particles.<sup>30</sup> However, it is still challenging to control the tip branching-level as a trace amount of AgNO<sub>3</sub> can cause a drastic change in the morphology of the thorny gold particles.<sup>8,27</sup> In addition, defects and impurities as well as seed concentration, pH, and temperature also were found to significantly influence the morphology of branched gold particles.<sup>30–33</sup>

Despite tremendous ongoing research on shape-controlled synthesis, the actual mechanism for the formation of branched gold structures is still under debate.<sup>30–33</sup> All these opportunities and challenges inspired us to systematically investigate the shape-controlled synthesis of complex multi-level branched mesoscale gold particles with optical excitations in the NIR/MIR spectral regions.

Herein, we report on a facile, aqueous based, one-step, and surfactant-free route for the synthesis of highly branched AuMFs. We found that halide ions Cl<sup>−</sup> played a crucial role during the growth of long and sharp tips by regulating the formation of multiple twin defects in the crystal structure of the growing particles. The lattice strain at the twin defects provides a driving force that facilitates tip elongation. It is noteworthy that the branching level of each tip was facilely tuned by adjusting the amount of halide ions Cl<sup>−</sup> added into the growth solution. Moreover, the effect of AgNO<sub>3</sub> and ascorbic acid on the morphology of branched AuMFs was also investigated. A tunable and extreme red shift of the LSPR peak position to ~1800–3000 nm was observed, depending on the morphology of the tips. We also conducted an optical simulation study based on the finite-difference time-domain (FDTD) method to provide an in depth understanding of the morphology-dependent optical properties and the EM field enhancement of highly branched AuMFs.

## Experimental section

### Materials

All chemicals were of reagent grades and used without purification. Tetrachloroauric acid trihydrate (HAuCl<sub>4</sub>·3H<sub>2</sub>O), silver nitrate (AgNO<sub>3</sub>), ascorbic acid (C<sub>6</sub>H<sub>6</sub>O<sub>6</sub>), sodium chloride (NaCl), sodium iodide (NaI), sodium bromide (NaBr), acetic acid, and chitosan (low molecular weight) were purchased from Sigma Aldrich.

### Synthesis of branched gold mesoflowers (AuMFs)

All the glassware was washed intensively with freshly prepared aqua regia solution (HCl:HNO<sub>3</sub> = 3:1 v/v) and rinsed thoroughly with milli-Q water before use. Briefly, 180 μL of HAuCl<sub>4</sub> (10 mM), 20 μL of AgNO<sub>3</sub> (10 mM), and 30 μL of HCl (1.0 M) were added into 3 mL of milli-Q water in a 20 mL glass vial. The mixture was magnetically stirred for 5 min at 700 rpm. Subsequently, 150 μL of ascorbic acid (10 mg mL<sup>−1</sup>) was rapidly added to the solution under vigorous stirring. The solution was kept stirring for further 4 min. To suspend the as-prepared particles, 1.4 mL of chitosan 1.0 wt% in 10 v/v% acetic acid solution was added drop-wise to

the above solution, followed by sonication for 1 min. The particles were then left undisturbed overnight. The purification step was carried out by three times of centrifugation at 3000 rpm in 10 min and washing with milli-Q water to remove all excess amounts of unbound chitosan and reagents prior to further characterization. The reaction was conducted at room temperature, under air exposure, and in a curtain-covered place. A lower yield synthesis of branched AuMFs was observed when the reaction was conducted in an extremely bright or dark place. To examine the effect of each reaction parameter on the morphology of the resulting particles, we altered the investigated parameter while fixing other reaction parameters.

### Characterization and simulation

The morphology and composition of AuMFs were characterized using a field emission secondary electron microscope (FESEM-6340F), a transmission electron microscope (TEM-JEOL 2010), an electron dispersive X-ray spectrometer (EDX-TEM-JOEL 2100), a dark-field scanning transmission electron microscope (STEM) and electron energy loss spectroscopy (EELS) using TEM-JOEL 2100. The crystallography information was studied by high-resolution transmission microscopy (HRTEM) using TEM-JOEL-2100 and X-ray diffraction spectroscopy (XRD). The XRD spectrum was recorded using a Shimadzu X-ray spectrometer equipped with a rotation anode. The Cu Kα source was used with a fixed power source of 2.0 kW at 40 kV and 30 mA. In a typical measurement, the sample was scanned at a rate of (1.5 deg min<sup>−1</sup>) over a range of 30° to 80°. The transmission spectra (*T*) of the AuMFs were measured using a UV-Vis-NIR spectrophotometer (Cary 5000). Extinction spectra were obtained from the transmission spectra as log(1/*T*). The finite-difference time-domain (FDTD) method<sup>34</sup> was used to study the optical properties and EM field distributions using a commercial package offered by Lumerical Solutions (FDTD solutions 8.6, Lumerical solutions, Inc., Vancouver, Canada). In all the calculations, the incident light used was a TFSF plane wave propagating along the *z*-axis and was polarized along the *x*-axis. Air was chosen as the surrounding medium for the calculation of the optical properties and EM enhancement. The mesh size used was 4 nm for spherical core and (*x* = 2.5 nm, *y* = *z* = 1 nm) for the tip. The dielectric function of bulk gold was obtained from CRC\* database.<sup>35</sup> The local EM field distributions were plotted using the log scale.

## Results and discussion

### Characterization of AuMFs

Branched AuMFs with a high density of long and sharp tips on the surface were synthesized in high yield at room temperature by a one-pot, aqueous-based, and surfactant-free approach. Briefly, an acidic solution (pH ~ 1–2) was used as the growth solution for the reduction of HAuCl<sub>4</sub> and AgNO<sub>3</sub> precursors by ascorbic acid. The reaction solution turned transparent immediately after adding ascorbic acid, indicating the reduction of Au<sup>3+</sup> ions to Au<sup>+</sup> ions.<sup>30</sup> After that, the suspension gradually changed into grey color (4 min of stirring), which was taken as a sign of

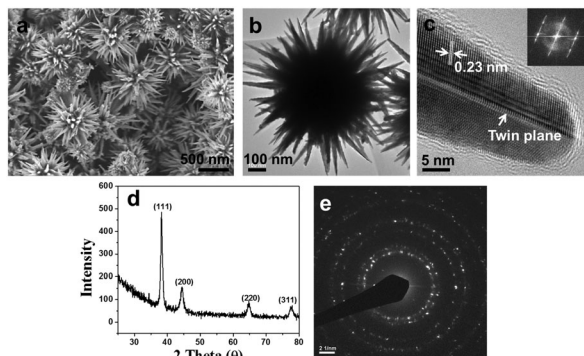


Fig. 1 (a) SEM, (b) TEM, and (c) HRTEM images and the inset FFT pattern of the tip, (d) XRD spectrum, (e) SAED pattern of branched AuMFs synthesized under typical conditions: 30  $\mu\text{L}$  HCl (1.0 M), 180  $\mu\text{L}$  HAuCl<sub>4</sub> (10 mM), 20  $\mu\text{L}$  AgNO<sub>3</sub> (10 mM), and 150  $\mu\text{L}$  ascorbic acid (10 mg mL<sup>-1</sup>  $\approx$  56 mM).

formation of AuMFs. The SEM and TEM images of the as-synthesized particles are shown in Fig. 1a and b, respectively. The dark contrast at the body center in the TEM image suggests that the branched AuMFs are composed of a solid core from which the tips grow.<sup>36,37</sup> A high density of  $\sim$ 200–300 nm long and sharp tips extend from the  $\sim$ 400 nm core particles. Noteworthy, the branched AuMFs in this study exhibit a higher density of long and sharp tips compared to those found in other reports on branched gold structures.<sup>1,7,9,38</sup> Moreover, a twin plane is observed along the tip growth direction with a  $d$ -spacing of  $\sim$ 0.23 nm which is assigned to the  $\{111\}$  reflections of fcc Au, Fig. 1c.<sup>25,27</sup> The FFT pattern (inset in Fig. 1c) indicates that the tip displays single crystalline character. However, the XRD spectrum, Fig. 1d, and the selected area electron diffraction (SAED) pattern, Fig. 1e, indicate that the resulting AuMFs (core plus tip) are poly-crystalline and dominated by  $\{111\}$  crystal facets. Moreover, the overlapping STEM-elemental mapping, Fig. S1a–d, and the EDX spectrum, Fig. S1e, demonstrate that branched AuMFs are primarily composed of Au with a trace amount of Ag randomly distributed throughout the particles (ESI<sup>†</sup>).

### Roles of halide

The synthetic protocol used for the branched AuMFs was modified from the seedless synthetic approach of gold nanostars reported earlier in the literature.<sup>27</sup> Importantly, the concentrations of HCl and HAuCl<sub>4</sub> in the growth solution were higher than those normally used in the reported synthetic protocols for gold nanostars.<sup>25,28,39</sup> It is anticipated that the presence of a high concentration of halide ions ( $\text{Cl}^-$ ) in the growth solution is responsible for the formation of highly branched AuMFs. To verify this hypothesis, a set of experiments were conducted where we systematically replaced HCl with approximate amounts of either H<sub>2</sub>SO<sub>4</sub> or a mixture of H<sub>2</sub>SO<sub>4</sub> and NaCl at fixed pH. When 15  $\mu\text{L}$  H<sub>2</sub>SO<sub>4</sub> (1.0 M) was used instead of 30  $\mu\text{L}$  HCl (1.0 M), gold nanostars with few tips on the surface were obtained, Fig. 2a. The obtained tips exhibit twin defects along the growth direction as observed in a previously reported work on gold nanostars,<sup>25</sup> and in Fig. S2 (ESI<sup>†</sup>). Interestingly, addition of 15  $\mu\text{L}$  H<sub>2</sub>SO<sub>4</sub> (1.0 M) with 30  $\mu\text{L}$  NaCl (1.0 M), Fig. 2b, led to the formation of

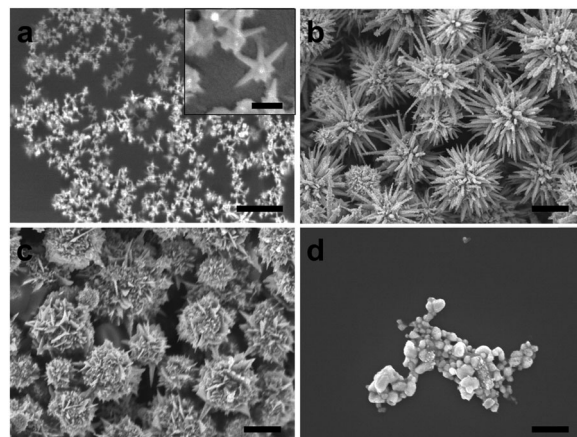


Fig. 2 SEM images of branched AuMFs synthesized under different conditions upon replacing 30  $\mu\text{L}$  of HCl (1.0 M) by: (a) 15  $\mu\text{L}$  H<sub>2</sub>SO<sub>4</sub> (1.0 M), (b) 15  $\mu\text{L}$  H<sub>2</sub>SO<sub>4</sub> (1.0 M) + 30  $\mu\text{L}$  NaCl (1.0 M), (c) 15  $\mu\text{L}$  H<sub>2</sub>SO<sub>4</sub> (1.0 M) + 30  $\mu\text{L}$  NaBr (1.0 M), and (d) 15  $\mu\text{L}$  H<sub>2</sub>SO<sub>4</sub> (1.0 M) + 30  $\mu\text{L}$  NaI (1.0 M). The inset scale bar in (a) is 100 nm and all other scale bars are 500 nm.

extensively branched mesoscale particles that possess a similar morphology to the branched AuMFs prepared in the presence of 30  $\mu\text{L}$  HCl (1.0 M), Fig. 1. We further studied the effect of other halides by replacing NaCl with the same amount of either NaBr or NaI. Fig. 2c and d show the SEM images of the particles prepared by adding 15  $\mu\text{L}$  H<sub>2</sub>SO<sub>4</sub> (1.0 M) with either 30  $\mu\text{L}$  NaBr (1.0 M) or 30  $\mu\text{L}$  NaI (1.0 M), respectively. Neither Br<sup>-</sup> nor I<sup>-</sup> ions were able to produce particles with long and sharp tips. For instance, Br<sup>-</sup> ions produced roughened gold mesoscale particles with a small number of long and sharp tips, whereas I<sup>-</sup> ions produced irregularly shaped gold nanoparticle aggregates/clusters without sharp tips. These results clearly indicate that the nature of the halide ion is crucial for the formation of mesoscale gold particles with a high density of long and sharp tips. The morphology and growth of AuMF are influenced by the type of halide ions mainly for three reasons. Firstly, the reduction potential of Au<sup>+</sup> to Au<sup>0</sup> is reduced with halides in the order  $\text{Cl}^- > \text{Br}^- > \text{I}^-$ . Secondly, the solubility of Au-halide complexes is reduced in the same order. Thus, the presence of Br<sup>-</sup> and I<sup>-</sup> ions can reduce the reaction rate compared to that of Cl<sup>-</sup> ions. Thirdly, the binding strength of the halide ion to Au decreases in the order  $\text{I}^- > \text{Br}^- > \text{Cl}^-$ . Thus Br<sup>-</sup> and I<sup>-</sup> ions are expected to block the exposed Au surface more efficiently which may inhibit the growth of gold nanoparticles into a flower shape.

To further explore the effect of the amount of Cl<sup>-</sup> ions on the morphology of branched AuMFs, a series of experiments were undertaken where the amount of NaCl added into the growth solution was varied while other reaction parameters were kept unchanged (30  $\mu\text{L}$  HCl 1.0 M, 180  $\mu\text{L}$  HAuCl<sub>4</sub> 10 mM, 20  $\mu\text{L}$  AgNO<sub>3</sub> 10 mM, and 150  $\mu\text{L}$  ascorbic acid 10 mg mL<sup>-1</sup>). Fig. 3 shows the corresponding SEM and TEM images of branched particles obtained by varying the volume of Cl<sup>-</sup> ions added from a NaCl stock solution (1.0 M). Interestingly, adding 30  $\mu\text{L}$  of NaCl led to the formation of branched AuMFs that exhibited a high density of sharp tips extending from the 400 nm core



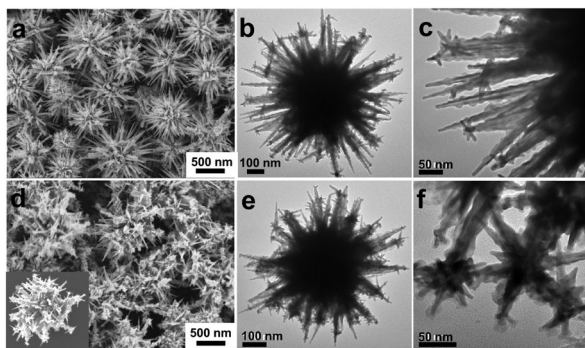


Fig. 3 SEM and TEM images of branched AuMFs synthesized at various concentrations of NaCl by adding different volumes of NaCl from a 1.0 M stock solution: (a–c) 30  $\mu$ L and (d–f) 60  $\mu$ L.

particles (about 400 tips per particle), Fig. 3a–c. The tips were sharp and the average length of each tip reached  $\sim 300$  nm. Small protrusions or secondary tips also appeared at the extremities of the long tips. Increasing the volume of  $\text{Cl}^-$  ions to 60  $\mu$ L prompted the elongation of the secondary tips on the primary tips, leading to the formation of multilevel branched AuMFs, Fig. 3d–f. The initiation and elongation of new tips on the previously formed tips induced by  $\text{Cl}^-$  ions did not stop at this stage. With a further increase in the added volume of  $\text{Cl}^-$  ions to 120  $\mu$ L, the hierarchy of branched AuMFs was further extended, with tertiary tips growing on the secondary tips and so on, Fig. S3 and S4 (ESI $^\dagger$ ).

The crystal structure of the tips with different branching levels obtained by varying the volume of NaCl in the growth solution is shown in Fig. 4. A 5-fold twinned defect at the tip extremity is observed in the primary long tip prepared without NaCl, Fig. 4a. The HRTEM images reveal that both primary tip and higher level tips grew parallel to the twin boundary along the  $\langle 11-2 \rangle$  direction with a  $d$ -spacing of 0.23 nm, which again is attributed to the  $\{111\}$  reflections of fcc gold, Fig. 4a–c.<sup>25,40</sup> Such a growth/tip elongation process has been observed before for related particles.<sup>8,25</sup> In the absence of twin defects, short tips are formed which often exhibit a single crystalline character.<sup>8,41</sup> The twin defects break the high symmetry of fcc crystals thus providing a driving force for the anisotropic growth of metal nanoparticles.<sup>37,42</sup> Therefore, incorporation of multiple twin

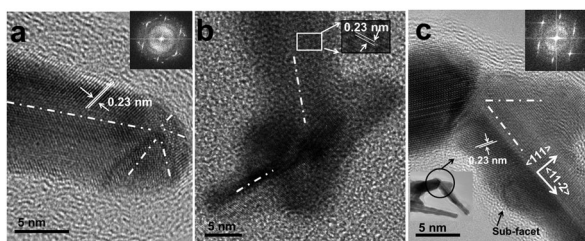


Fig. 4 HRTEM image of the tip with different branching levels prepared by varying the volume of NaCl added to the growth solution from a NaCl (1.0 M) stock solution: (a) 0  $\mu$ L, (b) 30  $\mu$ L, and (c) 60  $\mu$ L. The white dashed-lines indicate the twin defect planes. The inset FFT patterns are along the  $\langle 1-10 \rangle$  zone axis.

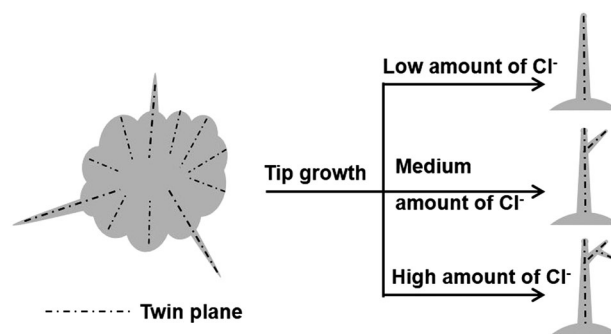
defects into the crystal structures of the growing particles results in the formation of highly branched tips. It is also worthwhile emphasizing that  $\text{Cl}^-$  ions are known to be mobile on the gold surface due to the weak interaction with gold.<sup>30</sup> This mobile character of  $\text{Cl}^-$  ions may regulate the formation of multiple twin defects in the crystal structure of the growing particles either by inducing disturbances in the atomic arrangement or by reducing the lattice strain in the twinned regions.<sup>12,43</sup>

As mentioned before, halides like  $\text{Br}^-$  and  $\text{I}^-$  ions are known to attach more strongly to gold surfaces than  $\text{Cl}^-$  ions.<sup>30,32</sup> Consequently, the addition of a large amount of halide ions,  $\text{Br}^-$  or  $\text{I}^-$  ions, might block the growth of gold nanoparticles leading to the formation of roughened gold mesoscale particles or irregularly shaped gold nanoparticles, respectively. Moreover, the presence of halide counter ions such as  $\text{H}^+$  and  $\text{Na}^+$  ions and the high concentrations of metal precursors might cause a dramatic aggregation of small nuclei during the growth process, thus promoting the formation of mesoscale particles of different shapes and morphologies.

Furthermore, time-dependent SEM images of the particles at different growth stages were also recorded to reveal the morphological evolution of branched AuMFs, Fig. S5 (ESI $^\dagger$ ). From this set of data and the observations in Fig. 1–4 we propose that nanoscale crystals formed in the growth solution aggregate into twin defect-rich solid cores from which the tips can grow into multilevel, highly branched mesoscale particles as schematically outlined in Scheme 1.

### Effect of $\text{AgNO}_3$

The role of silver ions  $\text{Ag}^+$  in the synthesis of branched gold nanoparticles is arguably reported since gold nanostars were obtained both in the presence<sup>8,27</sup> and absence of  $\text{Ag}^+$  ions.<sup>44</sup> The under potential deposition (UPD) of  $\text{Ag}^0$  on the surface of growing gold nanoparticles is supposed to alter the surface energy of different crystal facets and thereby dictate the morphology of the formed nanoparticles.<sup>30</sup> Besides, the presence of halide ions may affect the Ag UPD process by forming insoluble Ag-halide complexes or by competitively adsorbing on the gold surface and thereby stabilize/destabilize the  $\text{Ag}_{\text{UPD}}$  layer.<sup>30</sup> However, during the synthesis of branched gold nanoparticles, silver can adsorb on the gold surface in the form of  $\text{Ag}^0$  or  $\text{AgCl}$ .<sup>27,45</sup> To explore the effect of  $\text{AgNO}_3$  on the morphology of



Scheme 1 Proposed growth mechanism of AuMFs: the sharp tips grow from the twin defect planes and the concentration of  $\text{Cl}^-$  ions in the growth solution influences the tip morphology.

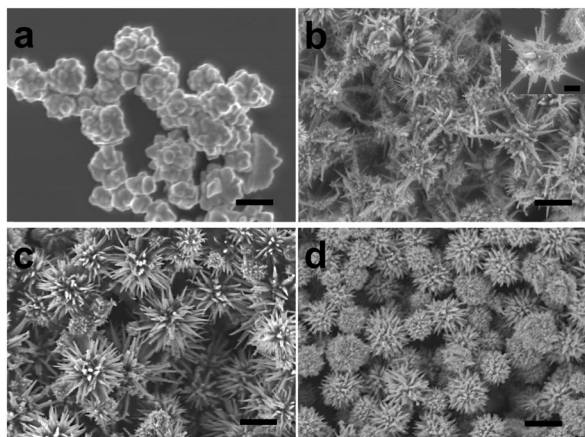


Fig. 5 SEM images of branched AuMFs synthesized by adding different volumes of  $\text{AgNO}_3$  from an  $\text{AgNO}_3$  stock solution (10 mM): (a) 0  $\mu\text{L}$ , (b) 10  $\mu\text{L}$ , (c) 20  $\mu\text{L}$ , and (d) 30  $\mu\text{L}$ . The inset scale bar is 200 nm and other scale bars are 500 nm.

branched AuMFs, we conducted a series of experiments by adding different volumes of  $\text{AgNO}_3$  from a stock solution (10 mM) while keeping other reaction parameters unchanged (30  $\mu\text{L}$  HCl 1.0 M, 180  $\mu\text{L}$   $\text{HAuCl}_4$  10 mM, and 150  $\mu\text{L}$  ascorbic acid 10  $\text{mg mL}^{-1}$ ), Fig. 5. In the absence of  $\text{AgNO}_3$ , gold sticky balls were obtained because of aggregation of small gold nanoparticles, Fig. 5a. Adding 10  $\mu\text{L}$  of  $\text{AgNO}_3$  resulted in the formation of branched AuMFs with long tips on the surface, Fig. 5b. Moreover, branched AuMFs with a high density of long and sharp tips on the surface were observed upon increasing the added volume of  $\text{AgNO}_3$  to 20  $\mu\text{L}$ , Fig. 5c. Upon further increasing the volume of  $\text{AgNO}_3$  to 30  $\mu\text{L}$ , the tips appeared to be shorter and less branched as compared to those obtained using 20  $\mu\text{L}$  of  $\text{AgNO}_3$ , Fig. 5d. In some parts of the image the particles appear roughened. These findings indicate that a trace amount of  $\text{AgNO}_3$  can cause a progressive change in the morphology of the obtained particles. However, due to the huge morphological sensitivity observed upon addition of a trace amount of  $\text{AgNO}_3$  it is advisable to utilize  $\text{Cl}^-$  ions to effectively and reproducibly control the morphology in the shape-controlled synthesis of multilevel branched AuMFs.

### Effect of ascorbic acid

Ascorbic acid is commonly used in the synthesis of anisotropic metal nanoparticles as a mild reducing agent.<sup>36</sup> To investigate the effect of ascorbic acid on the morphology of branched AuMFs, we conducted a series of experiments by adding different volumes of ascorbic acid from a stock solution (10 mM) into the growth solution while keeping other reaction parameters unchanged (30  $\mu\text{L}$  HCl 1.0 M, 180  $\mu\text{L}$   $\text{HAuCl}_4$  10 mM, and 20  $\mu\text{L}$   $\text{AgNO}_3$  10 mM), Fig. 6. Addition of a small volume of ascorbic acid (50  $\mu\text{L}$ ) yielded AuMFs with multiple leaf-like sheets extending from the core of the particles, Fig. 6a. Increasing the volume of ascorbic acid to 100 and 200  $\mu\text{L}$ , respectively, led to the formation of branched AuMFs with multiple long and sharp tips on the surface, which was attributed to a faster reaction rate, Fig. 6b and c. The tip size (width and length) and the synthesis

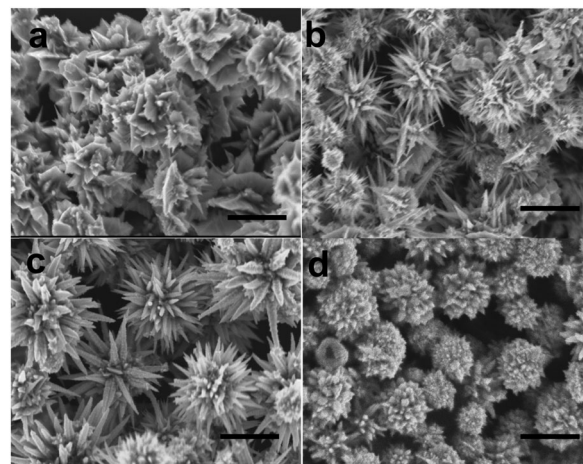


Fig. 6 SEM images of branched AuMFs synthesized by adding different volumes of ascorbic acid from an ascorbic acid stock solution (10  $\text{mg mL}^{-1}$ ): (a) 50  $\mu\text{L}$ , (b) 100  $\mu\text{L}$ , (c) 150  $\mu\text{L}$ , and (d) 450  $\mu\text{L}$ . All the scale bars are 500 nm.

yield also increased with increasing volumes of ascorbic acid. However, excessive amounts of ascorbic acid (450  $\mu\text{L}$ ) generated AuMFs with roughened morphology lacking sharp tips, Fig. 6d. The high reaction rate caused by the excess amount of ascorbic acid most likely resulted in the formation of a large number of nuclei in the growth solution. We anticipate therefore that the amount of  $\text{Au}^0$  atoms available in the growth solution is no longer enough to feed the elongation of the tips. The excessive amount of ascorbic acid may also induce a negative charge effect on the surface of the growing particles by adsorbing on the particle surface.<sup>33,39</sup> For instance, it might block the adsorption of  $\text{Cl}^-$  ions on the gold surface which is essential for the growth of multiple long and highly branched tips.

### Optical properties of AuMFs

To gain insights into the optical properties including the EM field distribution of the branched AuMFs, numerical simulations using the FDTD method were conducted. Three geometrical models of branched AuMFs numbered 1, 2, and 3, respectively, were considered to examine the effect of the tip morphology (sharpness and branching level) on their optical properties, Fig. 7. The 400 nm core particle was kept the same for the three models. In brief, the tip in model 2 shows a higher aspect ratio (length/width) compared with the features in model 1 (250/25 vs. 250/45). The tip in model 3 contains secondary small tips extending from the primary tip found in model 2 (so-called hyper-branched tip). The tip in model 1 can be found in the branched AuMFs in Fig. 1 (so-called AuMFs 1) and the tips in models 2 and 3 can be found in the branched AuMFs in Fig. 3 (so-called AuMFs 2 + 3). The simulated optical properties including the EM field enhancement for the three investigated models are shown in Fig. 8 and Table S1 (ESI†).

The extinction spectra are characterized by one pronounced red shifted peak in the NIR–MIR region ( $\sim 1500\text{--}3000$  nm), one distinct asymmetric peak in the NIR region ( $\sim 1100\text{--}1500$  nm), and several weak features located in the visible/NIR region ( $\sim 540$ , 635, and 860 nm), Fig. 8a. According to the literature,

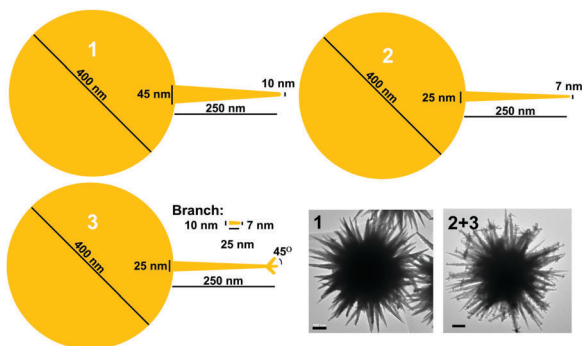


Fig. 7 Illustration of the models used in the simulations and the corresponding TEM images of AuMFs with long sharp and branched tips, respectively. Scale bars in the TEM images are 100 nm.

the extinction spectra of branched gold particles rely on the results of the hybridization of different plasmon modes corresponding to the core and individual tips.<sup>24,26</sup> High-order LSPR modes can be excited along with the dipolar LSPR mode located at the far-most wavelength upon increasing the size of particles or the length of tips.<sup>2</sup> Therefore, the weak features in the extinction spectra located at  $\sim 540$ , 635 and 860 nm could be assigned to the plasmon excitations of the hexadecapolar, octopolar, and quadrupolar LSPR modes of the 400 nm core particle. This observation is consistent with the findings for mesoscopic gold meatball particles reported by Wang *et al.*<sup>2</sup> Interestingly, an asymmetric peak located in the NIR region after a broad-continuum is observed in the extinction spectra for all three models. The overlapping of the broad dipolar plasmon mode (so-called superradiant) of the core particle and the narrow quadrupole plasmon mode (so-called subradiant) of the tip is accounted for the appearance of this Fano-type profile.<sup>46</sup> The Fano-resonance peak is of great interest in label-free LSPR sensing because of its unique shape.<sup>47,48</sup> Model 2 exhibits a

significant red shift of the LSPR peak position in MIR region compared to that of model 1, attributed to the higher aspect ratio tip. Notably, the longitudinal plasmon peak of gold nanorods was found to shift in a similar manner (towards longer wavelengths) upon increasing the aspect ratio (length/width) of the particles.<sup>49</sup> Model 3 causes a further red shift of the LSPR peak position compared to that of model 2, attributed to the hyper-branched tip. The corresponding experimental extinction spectra of branched AuMFs 1 and branched AuMFs 2 + 3 are shown in Fig. 8b. To avoid the strong absorbance of H<sub>2</sub>O in the NIR region, branched AuMFs were spread on a clean glass surface, dried completely under ambient conditions, and the measurement was conducted in air. The extinction spectrum of the branched AuMFs 1 is found at  $\sim 1800$  nm, whereas the extinction spectrum of the branched AuMFs 2 + 3 appears to reach its peak value in the 2500–3000 nm region. The results are in agreement with the far-most red shifted peaks in the simulated spectra. This is attributed to a variation in the morphology of the sample on the glass surface and/or of the individual particles in terms of tip size, sharpness and branching, which both contribute to the heterogeneous broadening seen in the experimental spectra.<sup>50</sup> However, we did not observe the high-order LSPR peaks located in the visible and NIR regions ( $\sim 1100$ –1500 nm) as displayed in the simulated spectra. The damping of the high-order LSPR peaks is attributed to the surface roughness of the real samples whereas the perfect smooth-surface core particle was used for simulation. The damping of the high-order LSPR peaks caused by surface roughness was also reported for gold meatball and nanoshell particles.<sup>2,51</sup>

The simulated EM field distributions for the three models in the MIR and NIR regions are shown in Fig. 8c. All three models exhibit a huge enhancement of the local EM field  $|E|^2$  of  $\sim 10^5$  and  $\sim 10^3$ – $10^5$  at the MIR and NIR resonance wavelengths, respectively.<sup>52</sup> The strongest EM field enhancement is found at the tip extremities, attributed to the sharp-tip effect.<sup>24</sup> Note that model 2 exhibits the greatest EM field enhancement and the largest hot-spot volume compared to model 1 and model 3. It is also worth pointing out that the hyper-branched tip in model 3 shifts the LSPR peak position to a longer wavelength at the expense of a slight reduction in the EM field enhancement and the hot-spot volume compared to those of model 2. This result is important to consider while designing complex metallic particles with the desired LSPR peak position and EM field enhancement. The EM field enhancements of branched AuMFs in this study are comparable to those of current high-performance SERS and SEIRA substrates fabricated by nanolithography techniques such as nano-gaps,<sup>53,54</sup> plasmonic nanoantennas,<sup>55</sup> bowtie antennas,<sup>56</sup> and recently fan-shape antennas.<sup>4</sup> Importantly, the abundant and open hot-spot areas of branched AuMFs that provide easy access for analytes offer great potential in applications such as surface enhanced vibrational spectroscopy and sensing/therapeutics.

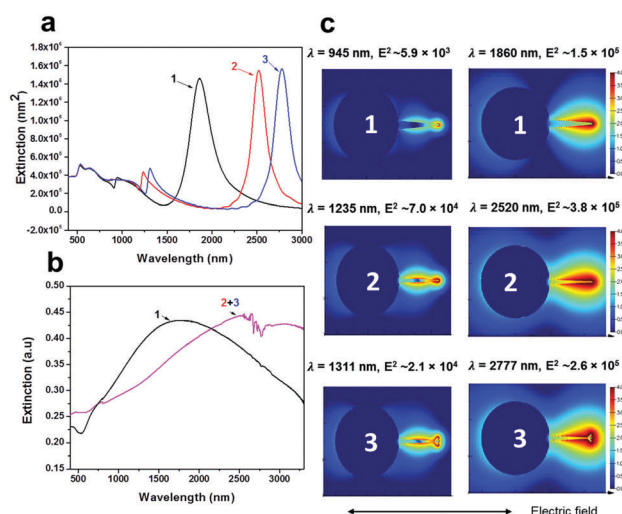


Fig. 8 (a) Simulated extinction cross section spectra of models 1, 2, and 3, (b) experimental extinction spectra of AuMFs 1 and AuMFs 2 + 3 and (c) simulated EM field enhancement of the three models at two resonance peaks. Polarization direction is indicated by the arrow.

## Conclusions

A facile, aqueous-based, seedless, and surfactant-free approach to synthesize highly branched AuMFs with a high density of



multilevel long and sharp tips on the surface is reported. The concentration of  $\text{Cl}^-$  ions played a decisive role in the formation of long and sharp tips by regulating the formation of multiple twin defects in the growing particles. Noteworthily, the branching level of each tip was facily tuned by adjusting the amount of  $\text{Cl}^-$  ions added into the growth solution. Other reaction parameters such as the amounts of  $\text{AgNO}_3$  and ascorbic acid were also found to influence the morphology of the particles primarily through manipulation of reaction kinetics and blocking of adsorption sites for the  $\text{Cl}^-$  ions. A tunable red shift of the LSPR peak position to the  $\sim 1800\text{--}3000$  nm region was observed, depending on the morphology of the tips. Simulations based on the FDTD method also revealed a significant EM field enhancement  $E^2$  of up to  $\sim 10^4\text{--}10^5$  at the MIR resonance wavelength as well as large hot-spot volumes. The clean synthesis and massively red shifted LSPR peak position toward the NIR-MIR region as well as the huge EM field enhancement make the AuMFs promising candidates for surface enhanced vibrational spectroscopy as well as for bio- and chemical sensing/photothermal applications. Thus, the proposed synthesis route offers great opportunities to facily produce novel complex mesoscale particles with advanced optical and structural properties.

## Acknowledgements

The authors acknowledge support from the School of Materials Science and Engineering and Provost Office of Nanyang Technological University. CP and BL also acknowledge support from the Nanomedicine Institute established by the collaboration of the Northwestern University and the Nanyang Technological University.

## Notes and references

- 1 J. Fang, S. Du, S. Lebedkin, Z. Li, R. Kruk, M. Kappes and H. Hahn, *Nano Lett.*, 2010, **10**, 5006–5013.
- 2 H. Wang and N. J. Halas, *Adv. Mater.*, 2008, **20**, 820–825.
- 3 L. Wang, H. Li, J. Tian and X. Sun, *ACS Appl. Mater. Interfaces*, 2010, **2**, 2987–2991.
- 4 L. V. Brown, X. Yang, K. Zhao, B. Zheng, P. Nordlander and N. J. Halas, *Nano Lett.*, 2015, **15**, 1272–1280.
- 5 F. Le, D. W. Brandl, Y. A. Urzhumov, H. Wang, J. Kundu, N. J. Halas, J. Aizpurua and P. Nordlander, *ACS Nano*, 2008, **2**, 707–718.
- 6 A. J. Blanch, M. Döbinger and J. Rodríguez-Fernández, *Small*, 2015, **11**, 4550–4559.
- 7 H. Yuan, W. Ma, C. Chen, H. Zhu, X. Gao and J. Zhao, *J. Phys. Chem. C*, 2011, **115**, 23256–23260.
- 8 H. Yuan, W. Ma, C. Chen, J. Zhao, J. Liu, H. Zhu and X. Gao, *Chem. Mater.*, 2007, **19**, 1592–1600.
- 9 P. R. Sajanlal and T. Pradeep, *Nano Res.*, 2009, **2**, 306–320.
- 10 A. Mayoral, C. Magen and M. Jose-Yacamán, *Cryst. Growth Des.*, 2011, **11**, 4538–4543.
- 11 D. Xu, J. Gu, W. Wang, X. Yu, K. Xi and X. Jia, *Nanotechnology*, 2010, **21**, 375101.
- 12 Y. Xia, Y. Xiong, B. Lim and S. E. Skrabalak, *Angew. Chem., Int. Ed.*, 2009, **48**, 60–103.
- 13 S. Boca, D. Rugina, A. Pinte, L. Barbu-Tudoran and S. Astilean, *Nanotechnology*, 2011, **22**, 55702–55709.
- 14 E. Martinsson, B. Sepulveda, P. Chen, A. Elfving, B. Liedberg and D. Aili, *Plasmonics*, 2014, **9**, 773–780.
- 15 P. Chen, N. T. Tran, X. Wen, Q. Xiong and B. Liedberg, *ACS Sens.*, 2017, **2**, 235–242.
- 16 C. L. Nehl and J. H. Hafner, *J. Mater. Chem.*, 2008, **18**, 2415–2419.
- 17 C. L. Nehl, H. Liao and J. H. Hafner, *Nano Lett.*, 2006, **6**, 683–688.
- 18 H. Chen, X. Kou, Z. Yang, W. Ni and J. Wang, *Langmuir*, 2008, **24**, 5233–5237.
- 19 J. Z. Zhang, *Optical properties and spectroscopy of nanomaterials*, World Scientific, 2009.
- 20 A. Guerrero-Martínez, S. Barbosa, I. Pastoriza-Santos and L. M. Liz-Marzán, *Curr. Opin. Colloid Interface Sci.*, 2011, **16**, 118–127.
- 21 Z. Liu, Z. Yang, B. Peng, C. Cao, C. Zhang, H. You, Q. Xiong, Z. Li and J. Fang, *Adv. Mater.*, 2014, **26**, 2431–2439.
- 22 L. Rodríguez-Lorenzo, R. A. Alvarez-Puebla, I. Pastoriza-Santos, S. Mazzucco, O. Stéphan, M. Kociak, L. M. Liz-Marzán and F. J. García de Abajo, *J. Am. Chem. Soc.*, 2009, **131**, 4616–4618.
- 23 K. M. Mayer and J. H. Hafner, *Chem. Rev.*, 2011, **111**, 3828–3857.
- 24 F. Hao, C. L. Nehl, J. H. Hafner and P. Nordlander, *Nano Lett.*, 2007, **7**, 729–732.
- 25 T. K. Sau, A. L. Rogach, M. Döbinger and J. Feldmann, *Small*, 2011, **7**, 2188–2194.
- 26 S. Trigari, A. Rindi, G. Margheri, S. Sottini, G. Dellepiane and E. Giorgetti, *J. Mater. Chem.*, 2011, **21**, 6531–6540.
- 27 L.-C. Cheng, J.-H. Huang, H. M. Chen, T.-C. Lai, K.-Y. Yang, R.-S. Liu, M. Hsiao, C.-H. Chen, L.-J. Her and D. P. Tsai, *J. Mater. Chem.*, 2012, **22**, 2244–2253.
- 28 A. Indrasekara, S. Meyers, S. Shubeita, L. Feldman, T. Gustafsson and L. Fabris, *Nanoscale*, 2014, **6**, 8891–8899.
- 29 K. A. Dick, K. Deppert, M. W. Larsson, T. Mårtensson, W. Seifert, L. R. Wallenberg and L. Samuelson, *Nat. Mater.*, 2004, **3**, 380–384.
- 30 M. L. Personick and C. A. Mirkin, *J. Am. Chem. Soc.*, 2013, **135**, 18238–18247.
- 31 R. G. Weiner, C. J. DeSantis, M. B. Cardoso and S. E. Skrabalak, *ACS Nano*, 2014, **8**, 8625–8635.
- 32 S. E. Lohse, N. D. Burrows, L. Scarabelli, L. M. Liz-Marzán and C. J. Murphy, *Chem. Mater.*, 2013, **26**, 34–43.
- 33 A. Kedia and P. S. Kumar, *J. Mater. Chem. C*, 2013, **1**, 4540–4549.
- 34 A. Taflove and S. C. Hagness, *Computational electrodynamics: the finite-difference time-domain method*, Artech House, Boston, 3rd edn, 2005.
- 35 J. Weaver and H. Frederikse, *Optical Properties of Metals and semiconductors*, *CRC Handbook of Chemistry and Physics*, CRC Press, Boca Raton, 74th edn, 1994, pp. 12-109–12-131.
- 36 L. Wang, C. Hu, Y. Nemoto, Y. Tateyama and Y. Yamauchi, *Cryst. Growth Des.*, 2010, **10**, 3454–3460.
- 37 X. W. Lou, C. Yuan and L. A. Archer, *Chem. Mater.*, 2006, **18**, 3921–3923.

- 38 F. Xu, K. Cui, Y. Sun, C. Guo, Z. Liu, Y. Zhang, Y. Shi and Z. Li, *Talanta*, 2010, **82**, 1845–1852.
- 39 W. Ahmed, E. S. Kooij, A. van Silfhout and B. Poelsema, *Nanotechnology*, 2010, **21**, 125605.
- 40 L. F. Zhang, S. L. Zhong and A. W. Xu, *Angew. Chem., Int. Ed.*, 2013, **52**, 645–649.
- 41 S. Maksimuk, X. Teng and H. Yang, *J. Phys. Chem. C*, 2007, **111**, 14312–14319.
- 42 J. L. Elechiguerra, J. Reyes-Gasga and M. J. Yacaman, *J. Mater. Chem.*, 2006, **16**, 3906–3919.
- 43 Y. Zheng, J. Zeng, A. Ruditskiy, M. Liu and Y. Xia, *Chem. Mater.*, 2013, **26**, 22–33.
- 44 W. Moukarzel, J. Fitremann and J.-D. Marty, *Nanoscale*, 2011, **3**, 3285–3290.
- 45 S. R. Jackson, J. R. McBride, S. J. Rosenthal and D. W. Wright, *J. Am. Chem. Soc.*, 2014, **136**, 5261–5263.
- 46 B. Luk'yanchuk, N. I. Zheludev, S. A. Maier, N. J. Halas, P. Nordlander, H. Giessen and C. T. Chong, *Nat. Mater.*, 2010, **9**, 707–715.
- 47 F. Hao, Y. Sonnefraud, P. V. Dorpe, S. A. Maier, N. J. Halas and P. Nordlander, *Nano Lett.*, 2008, **8**, 3983–3988.
- 48 C. Wu, A. B. Khanikaev, R. Adato, N. Arju, A. A. Yanik, H. Altug and G. Shvets, *Nat. Mater.*, 2012, **11**, 69–75.
- 49 L. Vigdeman, B. P. Khanal and E. R. Zubarev, *Adv. Mater.*, 2012, **24**, 4811–4841.
- 50 P. Chen and B. Liedberg, *Anal. Chem.*, 2014, **86**, 7399–7405.
- 51 H. Wang, G. P. Goodrich, F. Tam, C. Oubre, P. Nordlander and N. J. Halas, *J. Mater. Chem. B*, 2005, **109**, 11083–11087.
- 52 A. Li and S. Li, *Nanoscale*, 2014, **6**, 12921–12928.
- 53 X. Chen, C. Ciraci, D. R. Smith and S.-H. Oh, *Nano Lett.*, 2015, **15**, 107–113.
- 54 C. Huck, F. Neubrech, J. Vogt, A. Toma, D. Gerbert, J. Katzmann, T. Härtling and A. Pucci, *ACS Nano*, 2014, **8**, 4908–4914.
- 55 R. Adato and H. Altug, *Nat. Commun.*, 2013, **4**, 1–10.
- 56 N. A. Hatab, C.-H. Hsueh, A. L. Gaddis, S. T. Retterer, J.-H. Li, G. Eres, Z. Zhang and B. Gu, *Nano Lett.*, 2010, **10**, 4952–4955.